Published in final edited form as:
Neuroimage. 2011 April 1; 55(3): 1034–1043. doi:10.1016/j.neuroimage.2010.12.086.

Data-driven optimization and evaluation of 2D EPI and 3D PRESTO for BOLD fMRI at 7 Tesla: I. Focal coverage

Robert L. Barry[1,2,*], **Stephen C. Strother**[3,4], **J. Christopher Gatenby**[1,2,5], and **John C. Gore**[1,2,6]

[1]Vanderbilt University Institute of Imaging Science, Nashville, Tennessee, USA

[2]Department of Radiology and Radiological Sciences, Vanderbilt University Medical Center, Nashville, Tennessee, USA

[3]Rotman Research Institute, Baycrest, Toronto, Ontario, Canada

[4]Department of Medical Biophysics, University of Toronto, Toronto, Ontario, Canada

[5]Department of Radiology, University of Washington, Seattle, Washington, USA

[6]Department of Biomedical Engineering, Vanderbilt University, Nashville, Tennessee, USA

Abstract

Blood oxygenation level dependent (BOLD) functional magnetic resonance imaging (fMRI) is commonly performed using 2D single-shot echo-planar imaging (EPI). However, single-shot EPI at 7 Tesla (T) often suffers from significant geometric distortions (due to low bandwidth (BW) in the phase-encode (PE) direction) and amplified physiological noise. Recent studies have suggested that 3D multi-shot sequences such as PRESTO may offer comparable BOLD contrast-to-noise ratio with increased volume coverage and decreased geometric distortions. Thus, a four-way group-level comparison was performed between 2D and 3D acquisition sequences at two in-plane resolutions. The quality of fMRI data was evaluated via metrics of prediction and reproducibility using NPAIRS (Non-parametric Prediction, Activation, Influence and Reproducibility re-Sampling). Group activation maps were optimized for each acquisition strategy by selecting the number of principal components that jointly maximized prediction and reproducibility, and showed good agreement in sensitivity and specificity for positive BOLD changes. High-resolution EPI exhibited the highest z-scores of the four acquisition sequences; however, it suffered from the lowest BW in the PE direction (resulting in the worst geometric distortions) and limited spatial coverage, and also caused some subject discomfort through peripheral nerve stimulation (PNS). In comparison, PRESTO also had high z-scores (higher than EPI for a matched in-plane resolution), the highest BW in the PE direction (producing images with superior geometric fidelity), the potential for whole-brain coverage, and no reported PNS. This study provides evidence to support the use of 3D multi-shot acquisition sequences in lieu of single-shot EPI for ultra high field BOLD fMRI at 7T.

*Correspondence to: Robert L. Barry, Ph.D., Vanderbilt University Institute of Imaging Science, 1161 21st Avenue South, AA1105 Medical Center North, Nashville TN 37232-2310, Tel: (615) 322-0647, Fax: (615) 322-0734, robert.barry@vanderbilt.edu.

Keywords

functional magnetic resonance imaging (fMRI); blood oxygenation level dependent (BOLD) contrast; 7 Tesla; PRESTO (Principles of Echo-Shifting with a Train of Observations); reproducibility; prediction

INTRODUCTION

Functional magnetic resonance imaging (fMRI) at very high fields (7 Tesla (T) and beyond) should provide new information about brain function because of the increased signal-to-noise ratio (SNR) obtainable, coupled with an increased sensitivity to blood oxygenation level dependent (BOLD) signal changes (Ogawa et al., 1993; Gati et al., 1997). However, high field imaging also suffers from challenges such as the detrimental effects of larger-scale variations in magnetic susceptibility (Jezzard and Balaban, 1995) and less uniform radiofrequency (RF) fields (Vaughan et al., 2001). The advantages and constraints of different imaging methods are likely to be quite different at higher versus lower fields, and thus the temptation to adopt and translate methods that worked well at lower fields without re-evaluating other potential approaches should be avoided. In order to realize the full potential of higher fields, the questions of what are the optimal ways of acquiring and processing fMRI data to produce the highest quality activation maps need to be addressed. The pulse sequence commonly used to acquire functional images with T_2^*-weighting at 3T and below is 2D single-shot echo-planar imaging (EPI) (Mansfield, 1977; Mansfield et al., 1994). Advantages of 2D EPI include high efficiency in terms of SNR per unit time, immunity to some subject motion, and excellent BOLD sensitivity (Duyn et al., 1996). Disadvantages include geometric distortions in the presence of off-resonance effects (due to low bandwidth (BW) in the phase-encode (PE) direction) (Jezzard and Balaban, 1995) and the predominance of extraneous temporal variance from physiological processes (Weisskoff et al., 1993). Physiological noise is often proportional to the MR signal (Raj et al., 2000; Krüger and Glover, 2001), so it is amplified with increasing B_0 and counteracts gains in BOLD contrast-to-noise ratio (CNR) provided by the use of ultra high field magnets (Triantafyllou et al., 2005). Triantafyllou et al. (2006) proposed mitigating the relative importance of physiological noise by acquiring data at a high enough resolution so that the temporal SNR is dominated by thermal noise. BOLD CNR may then be significantly increased by smoothing images to the desired resolution instead of directly acquiring voxels matched to the lower resolution. However, acquiring single-shot echo-planar images with ~3 mm^3 voxels at 7T (Triantafyllou et al., 2005) for the sole purpose of mitigating the relative importance of physiological noise has four drawbacks: (1) the longer echo train required to traverse more of k-space further decreases BW in the PE direction, thereby amplifying geometric distortions; (2) the long echo train increases the minimum possible TE, which needs to be decreased at higher fields (typically at or slightly below T_2^*) to maximize BOLD contrast (Menon et al., 1993) and avoid excessive signal dephasing; (3) the number of slices that may be acquired within a typical volume acquisition time (VAT) of 1–4 sec (for a block design paradigm) is significantly decreased, thereby making a high-resolution acquisition strategy challenging for studies requiring whole-brain coverage; and (4) the high gradients and slew rates required to mitigate the previous three challenges increase the likelihood of undesirable peripheral nerve stimulation (PNS) (Reilly, 1989; Cohen et al., 1990). Since the pulse sequence (and associated acquisition parameters) selected to acquire functional data influences both the intrinsic quality of these data and the efficacy of post-acquisition processing steps to further improve data quality, alternatives to 2D single-shot EPI should be explored for ultra high field functional imaging.

Single-shot EPI is efficient because all of 2D k-space ($k_x \times k_y$) is acquired after a single RF pulse (with a relatively large flip angle) and little of the time involved in image acquisition is wasted. Alternatively, k-space may be acquired in two or more segments (so-called multi-shot imaging) using smaller flip angles and shorter repetition times. As an example, a fast low-angle shot (FLASH) sequence (Haase et al., 1986; Frahm et al., 1993) may be used to acquire one line of k-space per RF pulse. The advantage of 2D FLASH over 2D EPI is its relative immunity to off-resonance effects via accumulation of phase errors during the echo train readout because only one k_y line is acquired per excitation. Extensions of 2D gradient-echo EPI to three dimensions include 3D echo-volumar imaging (EVI) (Song et al., 1994; Mansfield et al., 1995) and 3D EPI (Poser et al., 2010). The goal of 3D single-shot EVI is to acquire all points in 3D k-space ($k_x \times k_y \times k_z$) after a single RF excitation, thereby making it the most extreme single-shot acquisition possible. The primary disadvantage of 3D EVI is that its very long echo train makes it especially vulnerable to geometric distortions (due to magnetic field inhomogeneities) in the second PE direction. The implementation of 3D EVI would also be challenging for ultra high field fMRI given the issues of decreasing T_2^* and limitations imposed on gradient strength and slew rates to avoid PNS. In 3D single-shot EPI, the same volume is excited multiple times and a single k-space plane ($k_x \times k_y$) is acquired after each excitation. 3D EPI benefits from volumetric averaging and the possibility of parallel imaging in two directions, and has been recently demonstrated as a viable alternative to 2D EPI for fMRI at 7T (Poser et al., 2010). Other methods have evolved in recent years that in theory come close in terms of their efficiency, and make use of other factors such as volumetric averaging to increase SNR. These 3D acquisitions can also achieve high image rates by using small flip angles, short TR values, and parallel imaging. One approach is a 3D multi-shot gradient echo acquisition, which has also been referred to as fast field echo (FFE) imaging (van der Meulen et al., 1985, 1988). In 3D FFE, a volume is excited and individual $k_x \times k_y$ planes are acquired in segments over multiple RF excitations (using small flip angles and repetition times). A parameter that must be selected for such sequences is echo train length (ETL), which determines the number of k-space lines acquired after each RF pulse. At one extreme (ETL = 1) only one line of k-space is acquired after an excitation, essentially becoming a 3D FLASH sequence (Koopmans et al., 2010). At the other extreme (ETL = k_y) the acquisition essentially becomes a 3D EPI. Another 3D sequence that may be used is PRESTO (PRinciples of Echo-Shifting with a Train of Observations) (Liu et al., 1993). The implementation of PRESTO is conceptually similar to that of FFE with the addition of extra dephasing and rephasing gradients to form the echo after a subsequent RF pulse (TR < TE). The benefit of echo shifting is a significant shortening of the VAT, which results in the acquisition of more functional volumes per run. Other alternative acquisition strategies employing small flip angles and short repetition times have been investigated, and include transition band (Miller et al., 2003, 2007) and passband (Bowen et al., 2005) steady-state free precession.

A recent 3T study by Neggers et al. (2008) found that 3D PRESTO implemented with sensitivity encoding (SENSE) (Pruessmann et al., 1999; Golay et al., 2000) offered superior BOLD CNR compared to 2D single-shot EPI. This result was attributed to improved temporal efficiency because echo shifting and parallel imaging in two directions resulted in the acquisition of four times as many functional volumes during each run. We have previously reported the use of 3D PRESTO and FFE with moderate ETLs and high SENSE factors to perform fMRI at 7T with high spatial and temporal resolution (Sexton et al., 2010). The preliminary results (from four healthy subjects) demonstrated slightly higher activation statistics for 2D EPI compared to 3D FFE at resolutions of $1.12 \times 1.12 \times 1.12$ mm^3 and $1.67 \times 1.67 \times 1.67$ mm^3, and slightly higher statistics for 3D PRESTO compared to 2D EPI at resolutions of $2.0 \times 2.0 \times 2.0$ mm^3 and $3.0 \times 3.0 \times 3.0$ mm^3 (Sexton et al., 2010). Our current work builds upon these results by (1) implementing data-driven metrics of prediction and reproducibility within a multivariate canonical analysis framework to

optimally de-noise fMRI data acquired using 3D PRESTO/FFE and 2D EPI at high (1.19 × 1.19 mm^2) and moderate (2.19 × 2.19 mm^2) in-plane resolutions, and (2) comparing these optimized data sets at the group level to demonstrate the potential benefits of using 3D PRESTO and FFE in lieu of 2D EPI for BOLD fMRI at 7T. A criterion of maintaining identical volume coverage for both in-plane resolutions necessitated partial brain coverage, so a robust visual stimulus was used to elicit activation in the primary visual cortex.

METHODS

Image Acquisition

A four-way comparison was performed between 2D single-shot EPI and 3D multi-shot acquisition strategies at two matching in-plane resolutions. Table 1 presents the parameters used for each acquisition strategy. The two k-space dimensions were 176 × 176 and 96 × 96, which (for a 210 × 210 mm^2 field of view (FOV)) resulted in 1.19 × 1.19 × 2 mm^3 and 2.19 × 2.19 × 2 mm^3 voxels, respectively. 3D PRESTO[1] was well suited to acquire 96 × 96 k-space. 3D FFE was used for 176 × 176 k-space because: (1) the implementation of PRESTO for this matrix size would have increased the minimum possible TE to significantly longer than what was desired (28 ms), and (2) if the ETL was reduced to compensate for the longer individual echoes, then the VAT would have been increased unacceptably. (Alternative implementations of 3D PRESTO are presented in the Discussion.) The TE and SENSE reduction factor (R) (Pruessmann et al., 1999) were matched across all four sequences. A TR of 2 s was selected for EPI, and the TR for FFE was set such that these three sequences had the same VAT. For PRESTO, the shifting of the echo and matching it to 28 ms resulted in a minimum VAT of just under a second; however, we elected to increase the VAT to 1 s to make a 2:1 ratio of PRESTO to EPI volumes. The flip angle used was 125% of the calculated flip angle (assuming T_1 = 1.90 sec for cortical gray matter at 7T (Wright et al., 2008)) to partially compensate for the “bulls eye” B_1 profile that is known to produce lower flip angles in the periphery of the brain (Vaughan et al., 2001). The volume coverage was determined by the maximum number of slices obtainable with the high-resolution sequences and kept constant across acquisition strategies. The ETL and resultant read/PE BWs are also reported.

Twelve volunteers were studied under a protocol approved by the Vanderbilt University Institutional Review Board. The twelve subjects (four males, 21–31 years; eight female, 19–46 years; 29.8±8.8 years) completed eight functional runs (two runs of each of the four acquisition strategies). Experiments were performed on a Philips 7T scanner with a quadrature transmit coil and 16-channel receive-only head coil (Nova Medical, Wilmington, MA). The scanner was operated with a maximum gradient strength of 33 mT/m and a maximum slew rate of 166 T/m/s. The visual paradigm was a block design with four segments of 24 s baseline (central fixation) and 24 s activation (stationary 8 Hz flashing checkerboard wedge (22.5°) in the left visual field). A whole-brain functional localizer with the same flashing checkerboard paradigm was used to both familiarize subjects with the stimulus and facilitate slice placement for the main experiment. The localizer was a 3D PRESTO sequence with the following parameters: FOV = 220 × 202 × 100 mm^3, 40 slices, 2.29 × 2.29 × 2.50 mm^3 voxels, TE = 24.54 ms, TR = 17.54 ms, θ = 10°, R = 2.4 in first PE direction and 1.5 in second PE direction (R_{total} = 3.6), ETL = 13, VAT = 2.0 s. Functional slices for the main experiment (12 × 2 mm thick = 2.4 cm coverage) were planned parallel to the calcarine sulcus through the volume of maximal activation as identified by the localizer. The shim volume covered the posterior third of all slices to avoid the frontal sinuses and achieve a better shim in the occipital lobe. The whole-brain T_1-weighted anatomical (1 × 1 ×

[1]What we refer to as simply ‘PRESTO’ has been called ‘PRESTO-SENSE’ by previous authors.

1 mm^3 voxels, 192 slices, TE/TR = 1.88/4.2 ms, θ = 7°, R = 2.87, 7 min) was acquired during planning of the functional slices. The four functional sequences (A, B, C, D) were implemented with maximum spacing between repeated runs and different (pseudorandomized) permutations across subjects with the goal of balancing the influence of subject attention and fatigue across acquisition strategies. For example, the order of runs for subject #1 was (A1, B1, C1, D1; A2, B2, C2, D2), the order of runs for subject #2 was (D1, C1, B1, A1; D2, C2, B2, A2), and so on.

Data Processing

The workflow for data processing and analysis was automated using software written in Matlab (MathWorks, Natick, MA). Preprocessing was performed using AFNI (Cox, 1996). Binary masks of the brain were created (`3dAutomask`) for each functional run using an iterative algorithm (`3dClipLevel`) to select a threshold separating brain from background noise. Each mask was visually verified to retain cortical gray matter, and voxels included only in both masks (for each pair of runs) that were also within the shim volume were retained for subsequent analyses. The masked functional data were spatially smoothed (`3dmerge`) with seven full-width-at-half-maximum (FWHM) kernel sizes (7, 9, 11, 13, 15, 17, 19 mm) in the range of values appropriate for group analyses (Strother et al., 2004; Mikl et al., 2008). Each subject's anatomical volume was transformed (`3dWarp, @auto_tlrc`) into MNI space (ICBM-152); the same transformation parameters were then applied (`adwarp`) to masked functional volumes, resulting in 2 × 2 × 2 mm^3 voxels in MNI space. MRIcron (http://www.cabiatl.com/mricro/mricron) was used after transformations to visually verify the good overlay of functional data on the anatomical within the shimmed region. Although numerous post-acquisition algorithms and techniques to improve data quality are available (Strother, 2006) and could have been used, this study focused on the effects of spatial smoothing and estimation of the intrinsic data dimensionality (discussed in the next section) because these two steps have been shown (Strother et al., 2004; Yourganov et al., in press) to be crucial in optimizing the fMRI data-processing pipeline.

NPAIRS

The quality of fMRI data was evaluated via data-driven metrics of *prediction* and *reproducibility* using NPAIRS[†] (Non-parametric Prediction, Activation, Influence and Reproducibility re-Sampling) (Strother et al., 2002,2010). Reproducibility ($r \in [0,1]$) measures the similarity (Pearson correlation coefficient) of activation maps generated from two independent data sets, and is monotonically related to the global (statistical parametric map) SNR ($r \to 1$ as SNR $\to \infty$) (as defined in Strother et al., 2002;LaConte et al., 2003). Prediction ($p \in [0,1]$) originates from the field of statistical learning theory and evaluates the degree (e.g., posterior probability) to which a trained model can assign correct class labels (e.g., 'baseline' and 'activation') to an independent test set. Since the current study has only two classes, $p \in [0.5,1]$ where the lower bound represents the probability of randomly assigning a correct class label (50%). For EPI and FFE data, 79 volumes were assigned to either 'baseline' or 'activation' after discarding the first 2 volumes (approaching steady-state magnetization) and 15 transition volumes (between baseline and activation); similarly for PRESTO data, 158 volumes were retained after discarding 5 initial volumes and 29 transition volumes. Each pair of runs (with identical acquisition parameters) was grouped as a session to create four sessions per subject (one for each acquisition strategy) and twelve sessions per acquisition strategy (one for each subject).

The implementation of NPAIRS used principal component analysis (PCA) as an initial feature selection step to capture functional connectivity through the covariance structure,

[†]NPAIRS is freely available at http://code.google.com/p/plsnpairs

resulting in 1,896 principal components (PCs) for EPI/FFE (12 subjects × 79 retained volumes / run × 2 runs) and 3,792 PCs for PRESTO (12 subjects × 158 retained volumes / run × 2 runs). A denoised subspace consisting of 30% of these PCs was retained for the subsequent split-half resampling and canonical variate analysis (CVA). For each acquisition strategy, the re-sampling process split the twelve sessions into two equal groups of six (with a maximum of $^{12}C_6 / 2 = 462$ possible splits). A second PCA was performed on the independent groups for each split, and a variable number of PCs were used for each CVA – effectively implementing a penalized discriminant analysis (PDA) with subspace size as the penalizing hyperparameter (e.g., Kustra and Strother, 2001). Ideally only the PCs that represent variance due to group BOLD signal changes would be retained for the PDA (i.e., PCA denoising and penalization); however, selecting an appropriate number of PCs through analytical or empirical estimates (Hansen et al., 1999) is a non-trivial task: too few PCs fail to properly capture the true complexity of BOLD signal changes (excessive bias) whereas too many PCs include extraneous noise (excessive variance) (Geman et al., 1992) in the time series (Yourganov et al., in press). This study considered 52 inclusive ranges of PCs (1–2, 1–3, …, 1–49, 1–50, 1–75, 1–100, 1–150) to investigate all lower PCs that could contain BOLD-related variance, and the effect that including each additional high-order PC has on *p* and *r*. All possible splits (462) were considered for PC ranges up to and including 1–20 (for EPI) or 1–50 (for FFE/PRESTO), and 50 splits were used for all higher PC ranges to control total computation time. For each split, reproducibility was calculated on the composite activation maps from the two independent groups, and prediction was the mean classification accuracy achieved when the statistical model was trained using the first group and tested on the second, and then trained using the second group and tested on the first. Reported values for prediction and reproducibility were the median prediction and reproducibility across all split-half samples.

Each (prediction, reproducibility) pair, (*p*,*r*), reflects the end result of all (acquisition and processing) pipeline choices, including any interactions between parameters and/or steps, for a given range of PCs. Noiseless fMRI data with a perfect model would be mapped to (*p*=1,*r*=1). If equal weightings are given to prediction and reproducibility, as is done in this study, then the Euclidean distance $\sqrt{(1-r)^2+(1-p)^2}$ between (*p*,*r*) and the optimal point at (1,1) may be minimized to select an appropriate number of PCs for each acquisition-processing pipeline.

RESULTS

Figure 1 presents unprocessed anatomical and functional images from one representative subject. Fig. 1A is the high-resolution anatomical corresponding to the middle (seventh) functional slice (parallel to the calcarine sulcus). The rectangle depicts the approximate placement of the shim volume through this slice (to achieve a good shim in the primary visual cortex). Fig. 1(B–E) shows the middle functional slice from the first volume acquired using: (B) high-resolution (HR)-EPI, (C) low-resolution (LR)-EPI, (D) FFE, and (E) PRESTO. The outline of the brain (excluding dura, most notably in the anterior region) in (A) is superimposed on each functional image to better visualize geometric distortions in the PE direction (left to right). As predicted by their respective PE BWs, the functional images acquired using EPI exhibit more severe geometric distortions (both stretching and shearing) than the analogous multi-shot approaches. A visual comparison between Fig. 1(B–E) and the anatomical shows that: (1) the HR-EPI image has a left shift of ~3–4 pixels within the shim volume and distortions on the order of a centimeter or more in anterior regions; (2) the LR-EPI image has shifts of ~2–3 pixels within the shim volume and distortions akin to HR-EPI outside the shim volume; (3) the FFE image has shifts of ~1–3 pixels within the shim volume; and (4) the PRESTO image has shifts of ~1 pixel or less within the shim volume.

Both 3D acquisitions also exhibit much less severe distortions outside the shim volume than their 2D counterparts.

Figure 2(A–D) plots (*p*,*r*) for all 1,456 NPAIRS analyses (4 acquisition strategies × 7 spatial smoothing (SS) kernels × 52 PC ranges). Line segments connect consecutive (*p*,*r*) points as the PC range increases from 1–2 to 1–150. Each of these 28 curves (7 per subplot) depicts the trajectory through (*p*,*r*)-space for a unique acquisition-processing pipeline, and has a single point with minimal Euclidean distance to (1,1). This point is identified for each trajectory and displayed in Fig. 2E. The number of PCs retained at the point closest to (1,1) represents the optimal balance between bias and variance that jointly maximizes prediction and reproducibility. Figure 2(Az–Dz) magnifies clusters in Fig. 1E for each acquisition sequence in Fig. 2(A–D) to clearly show the SS kernel and number of PCs associated with each point, and the relative distance between points.

Each point in (*p*,*r*)-space represents a unique activation map that reflects one of the 1,456 acquisition-processing-denoising pipelines, and an activation map constructed from one of the 28 optimal (*p*,*r*) points (in Fig. 2E) is expected to be of the highest quality possible (balancing bias and variance) for the specified acquisition-processing pipeline. Figure 3 displays group activation maps associated with optimal (*p*,*r*) (identified by arrows in Fig. 2(Az–Dz)) for data processed with the median SS kernel (13 mm FWHM). These maps are presented with a common threshold of $|z| > 5$ and dynamic range from $z = -6.670$ (blue) to $z = 18.99$ (dark red). Very good agreement in both sensitivity and specificity is observed for contralateral BOLD activation, as well as a robust ipsilateral 'negative' BOLD response (Tootell et al., 1998;Shmuel et al., 2002;Smith et al., 2004).

Figure 4 presents six scatter-plot comparisons for the unthresholded data sets used to generate Fig. 3: (A) HR-EPI vs. LR-EPI; (B) HR-EPI vs. FFE; (C) HR-EPI vs. PRESTO; (D) FFE vs. LR-EPI; (E) PRESTO vs. LR-EPI; and (F) PRESTO vs. FFE. A point above the line of unity reflects a voxel (within both image masks) exhibiting a higher group z-score with the acquisition sequence labeled on the vertical axis than the acquisition sequence labeled on the horizontal axis. For each comparison, the mean ratio of z-scores across highly significant voxels ($z > 7$ in one or both of the acquisition sequences) may be used as a scalar metric to quantify the increase in statistical significance for BOLD activation. For these group analyses (using a SS kernel of 13 mm FWHM): HR-EPI has a 20.3% increase over LR-EPI, a 19.8% increase over FFE, and a 15.1% increase over PRESTO; FFE has a 7.50% increase over LR-EPI; and PRESTO has a 4.55% increase over FFE and a 9.73% increase over LR-EPI. These six comparisons are repeated for each SS kernel and summarized in Table 2. Across all seven kernels, HR-EPI exhibits higher z-scores in the most number of comparisons (20), followed by PRESTO (15), FFE (4), and finally LR-EPI (3).

DISCUSSION

We have demonstrated the feasibility of using 3D PRESTO for BOLD fMRI at 7T using an optimization and evaluation of functional data based upon NPAIRS metrics. Metrics of prediction and reproducibility were employed to estimate the intrinsic data dimensionality (number of PCs) for each acquisition-processing pipeline. Activation maps constructed with optimized data showed very good agreement in sensitivity and specificity across acquisition strategies. Voxel-wise comparisons within the intersecting region of active foci revealed higher group z-scores for 3D PRESTO than 2D EPI acquired with ~$2 \times 2 \times 2$ mm^3 voxels. In fact, LR-EPI produced some of the lowest z-scores overall, and outperformed only FFE when a moderate SS kernel (7–11 mm FWHM) was used. This observation is particularly interesting because single-shot EPI is still the pulse sequence of choice for most 7T fMRI studies. The analyses of EPI data acquired at two resolutions (2.83 mm^3 and 9.59 mm^3) also

confirmed previous work stating that amplified physiological noise at ultra high fields can be mitigated by acquiring EPI data in a regime where voxels are dominated by thermal noise (~3 mm^3 at 7T) and then smoothing to the desired resolution to increase BOLD CNR (Triantafyllou et al., 2005, 2006).

The use of low flip angles in PRESTO reduces the relative significance of physiological noise. Similarly, for FFE, low flip angles and smaller voxels both contributed to the decrease in relative contributions of physiological noise. BOLD CNR was then recovered through the local spatial averaging of thermal noise (Lowe and Sorenson, 1997). The temporal efficiency of PRESTO provided a further increase in statistical power because twice as many functional volumes were acquired during each run.

A range of smoothing kernels was considered for this study because the optimal kernel width for these data (as suggested by matched filter theory (Rosenfeld and Kak, 1982)) is not known *a priori*, and previous reports have highlighted the benefits of using more than one kernel width when analyzing and interpreting functional data (Poline and Mazoyer, 1994a, 1994b; Worsley and Friston, 1995; Worsley et al., 1996; Skudlarski et al., 1999; LaConte et al., 2003; Shaw et al., 2003; Strother et al., 2004; Weibull et al., 2008). The seven SS kernels spanned a range between what is typically used in the literature for group analyses (~7 mm FWHM) to account for anatomical and functional heterogeneity across subjects (Galaburda et al., 1990; Mikl et al., 2008) and group alignment issues (Hellier et al., 2003), to what may be considered an upper limit (~19 mm FWHM) to maximize prediction and/or reproducibility (Strother et al., 2004) (although Mikl et al. (2008) investigated smoothing up to 30 mm FWHM). As per Table 2, the mean improvement in group z-scores for PRESTO vs. LR-EPI monotonically increased from 3–4% (7–9 mm) to 24–26% (17–19 mm). A marginal improvement of ~3% may be expected for relatively narrow kernel widths because the benefits of SS have not been fully realized (Strother et al., 2004; Triantafyllou et al., 2006), but this improvement further increased to 7–10% for a moderate degree of smoothing (11–13 mm). Group analyses such as these are performed in most neuroimaging studies because they identify group-level activations that are expected to be representative of the larger population. Single-subject analyses may also be performed to identify subject-specific activation signatures; however, choosing an appropriate SS kernel size for individual subjects is non-trivial because the optimal value has been shown to vary both between subjects (Shaw et al., 2003) and between activated foci of different sizes within subjects (Poline et al., 1997; McGonigle et al., 2000). Therefore, we expect that single-subject analyses of high-resolution data (without group alignment) would yield optimized pipelines at lower smoothing values down to and including no smoothing (Shaw et al., 2003).

The ability to detect statistically significant BOLD signal changes that reveal new insight into the functioning of the human brain is an unquestionably important criterion for any fMRI study, and is the primary reason for going to higher fields (Ogawa et al., 1993; Gati et al., 1997). Another very important consideration when selecting a pulse sequence and associated acquisition parameters is the vulnerability of functional images to geometric distortions. A well-known disadvantage of single-shot EPI is that it is highly susceptible to image distortions (Jezzard and Balaban, 1995) that obscure the natural coupling between functional activation and underlying anatomy. In this study, LR-EPI had a PE BW of 42.5 Hz. In comparison, the PE BW for PRESTO was 142.5 Hz – over 3.3 times higher than LR-EPI. As illustrated in Fig. 1, this higher BW translated into pixel shifts that were less than one-third as severe in PRESTO compared to LR-EPI, resulting in functional volumes with superior geometric fidelity. The use of PRESTO to mitigate such distortions would also be of particular importance for single-subject analyses where shifts of ~3 pixels in functional

images can make gray matter activation appear in white matter or outside the brain when overlaid on the underlying anatomy.

The fact that HR-EPI demonstrated the highest z-scores suggests that 2D EPI may still be appropriate for some high-resolution fMRI studies (with ~1 × 1 × 2 mm^3 or smaller voxels) that require extra sensitivity to detect subtle BOLD signal changes. However, this heightened sensitivity comes at the price of the lowest PE BW (20.0 Hz), resulting in the worst geometric distortions of the four acquisitions strategies (as per Fig. 1B). In comparison, the high-resolution implementation of 3D FFE had a PE BW of 42.6 Hz – over 2.1 times higher than HR-EPI. The extra sensitivity to BOLD changes may not be crucial for paradigms that are known to produce robust activation (e.g., a flashing checkerboard wedge, finger tapping, etc.), and thus trading extra sensitivity for increased geometric fidelity (as per Fig. 1D) would certainly be a worthwhile consideration for many studies (e.g., polar angle retinotopic mapping (Sexton et al., 2010)).

In addition to z-scores and geometric distortions, a tertiary consideration that should not be overlooked is the likelihood that a pulse sequence will produce PNS (Reilly, 1989; Cohen et al., 1990). Although not harmful, PNS should be avoided whenever possible because it decreases subject comfort (increasing the likelihood of movement and reduced task performance) and is clearly a complication for studying cognitive brain responses (e.g., associated with attention). The manifestation of PNS was described in the protocol and verbally reinforced to each volunteer before being placed in the scanner. In addition to having the most severe geometric distortions, HR-EPI was also the only acquisition sequence that subjects reported experiencing some form of PNS.

As previously mentioned, one of the advantages of 3D acquisitions is the ability to perform SENSE acceleration in both PE directions (e.g., Neggers et al., 2008; Poser et al., 2010). However, it has been observed (Sexton, 2010) that a minimum volume coverage of ~80 mm may be required to avoid excessively high g-factors (Pruessmann et al., 1999) when also accelerating in the second PE direction. We therefore elected to apply SENSE acceleration in only the first PE direction as this study had focal volume coverage (24 mm), although 3D PRESTO with SENSE acceleration in both PE directions is certainly possible at 7T as demonstrated by our whole-brain functional localizer.

It must be noted that we are aware of a recent claim that “PRESTO is not a viable option at 7T and higher particularly when high spatial resolution is desired, as the typically short TE will not leave enough time for acquiring the shifted echo from the previous excitation” (Poser et al., 2010). While it is true that the echo shifting places restrictions on the maximum obtainable resolution for a desired TE, this point does not preclude the use of PRESTO at ultra high fields. In this study, the k-space matrix size was increased from 96 × 96 to 176 × 176 for high-resolution acquisitions, which is more than a three-fold increase in the number of k-space points. A shifting of the echo for this 176 × 176 acquisition (keeping all other parameters constant) would have resulted in a minimum TE of 49 ms, which was too high for our application; this is the reason why we switched to a 3D FFE. However, this does not mean that PRESTO cannot be used for higher resolution applications: decreasing the matrix size slightly to 144 × 144 (a 1.46 × 1.46 mm^2 in-plane resolution for our FOV, or a 1.33 × 1.33 mm^2 in-plane resolution for a 19.2 × 19.2 cm^2 FOV) with ETL = 11 and R = 3.41 would have resulted in a minimum TE of 29 ms (and VAT = 1.2 s), which is only 1 ms longer than the TE used in this study and an acceptable value for gradient-echo fMRI at 7T. Another important observation is that PRESTO was in fact able to achieve a minimum TR of 12 ms, a minimum TE of 17 ms, and a minimum VAT of 527 ms for the 96 × 96 k-space acquisition (keeping all other parameters constant). However, as a criterion of this study was to keep TE constant across acquisition strategies, and the lowest TE achievable with the

high-resolution acquisitions was 28 ms, we had to increase TE (and thus VAT) for the PRESTO acquisition. It is therefore likely that the z-scores reported for PRESTO (although on average already higher than LR-EPI) underestimate its full potential for this application because nearly twice as many *more* volumes (a 3.80:1 ratio of PRESTO to EPI volumes) could have been acquired if a shorter echo time had been used. This observation is attributed solely to increased temporal efficiency through echo shifting because both sequences utilized the same SENSE acceleration factor. Therefore, based upon the results presented herein (and other unpublished observations), we disagree with the aforementioned claim and believe that PRESTO has considerable potential for fMRI at field strengths of 7T and higher.

Previous works have employed NPAIRS to analyze BOLD fMRI data acquired at 1.5T (LaConte et al., 2003; Shaw et al., 2003, 2009; Evans et al., 2010) and 3T (Shaw et al., 2003; Chen et al., 2006). This paper demonstrates the first use of NPAIRS to evaluate data acquired at 7T. Furthermore, whereas previous methodological studies have investigated PCA denoising (Andersen et al., 1999; Thomas et al., 2002), the acquisition-processing pipeline without PCA denoising (Triantafyllou et al., 2006), and the processing-denoising pipeline for a single acquisition strategy (LaConte et al., 2003; Shaw et al., 2003, 2009; Strother et al., 2004; Chen et al., 2006; Zhang et al., 2009; Evans et al., 2010), we believe that this paper is also the first investigation of simultaneously optimizing all three components of the acquisition-processing-denoising pipeline. This is an important step forward because these previous studies have shown that (1) interactions occur between sequential steps in the pipeline, and (2) optimizing a subset of the pipeline will likely result in a global pipeline optimization that converges on a local maximum. For example, if this study had acquired data only using LR-EPI, then potential statistical gains offered by PRESTO would not have been discovered. However, a key difference between data acquisition and processing/denoising is that whereas data processing/denoising only requires a computer and an arbitrary period of time to explore hundreds or thousands of processing-denoising combinations, the acquisition stage of an fMRI study is typically limited to 30–45 min of useful scan time. Furthermore, as other preprocessing steps (e.g., to compensate for physiological noise, geometric distortions, slice timing differences, and subject motion) will be considered in future studies, it must also be noted that such algorithms have been developed and validated primarily using 2D EPI data. The efficacy of most algorithms may be unchanged between 2D and 3D data, but some algorithms may have specific design assumptions related to the 2D acquisition that preclude their use on 3D data. Thus, confirming the efficacy of certain preprocessing algorithms for use on 3D data, as well as exploring potential interactions between sequential processing steps (Barry et al., 2010), remain topics for further consideration.

Finally, this work utilized NPAIRS metrics to objectively estimate the intrinsic data dimensionality for each acquisition-processing combination (Fig. 2E) by identifying the (p,r) point with minimal Euclidean distance to (1,1). However, the (p,r) trajectories presented in Fig. 2(A–D) possess rich and complicated structures that reveal similarities, differences, and interactions across acquisition sequences, and suggest that selecting a single point believed to be optimal is only part of a larger story. A detailed investigation of such (p,r) trajectories is ongoing and will be presented in a future report.

CONCLUSIONS

This study provides evidence to support the use of 3D multi-shot acquisition sequences such as PRESTO in lieu of single-shot EPI for ultra high field BOLD fMRI at 7T. Data-driven NPAIRS metrics were used to estimate the intrinsic data dimensionality for each acquisition-processing pipeline and thus provide an unbiased comparison between

acquisition strategies. Although high-resolution EPI exhibited the highest group z-scores of the four acquisition strategies considered, it came at the cost of significant geometric distortions, limited volume coverage, and PNS. In comparison, 3D PRESTO also had high z-scores (higher than EPI for a matched in-plane resolution), the potential for whole-brain coverage, and no reported PNS – suggesting that it may be preferable to 2D EPI for whole-brain fMRI at 7T. Future work will compare EPI and PRESTO for other paradigms under the criterion of identical whole-brain coverage, as well as extend the methodologies to include within-subject optimization, single-subject analyses, and Gaussian naïve Bayes classification.

Acknowledgments

This research was supported by NIH grant 5R01EB000461 to John C. Gore and CIHR/MOP84483 to Stephen C. Strother, who also gratefully acknowledges support of the Heart & Stroke Foundation of Ontario through the Centre for Stroke Recovery. The authors thank Baxter Rogers and Allen Newton for helpful discussions, and Anita Oder for her assistance in implementing the Java version of NPAIRS.

REFERENCES

Andersen AH, Gash DM, Avison MJ. Principal component analysis of the dynamic response measured by fMRI: a generalized linear systems framework. Magn. Reson. Imag 1999;17:795–815.

Barry RL, Williams JM, Klassen LM, Gallivan JP, Culham JC, Menon RS. Evaluation of preprocessing steps to compensate for magnetic field distortions due to body movements in BOLD fMRI. Magn. Reson. Imag 2010;28:235–244.

Bowen, CV.; Menon, RS.; Gati, JS. High field balanced-SSFP fMRI: a BOLD technique with excellent tissue sensitivity and superior large vessel suppression. Proc. 13th Scientific Meeting of the ISMRM; Miami Beach, Florida. 2005. p. 119

Chen X, Pereira F, Lee W, Strother S, Mitchell T. Exploring predictive and reproducible modeling with the single-subject FIAC dataset. Hum. Brain Mapp 2006;27:452–461. [PubMed: 16565951]

Cohen MS, Weisskoff RM, Rzedzian RR, Kantor HL. Sensory stimulation by time-varying magnetic fields. Magn. Reson. Med 1990;14:409–414. [PubMed: 2345521]

Cox RW. AFNI: software for analysis and visualization of functional magnetic resonance neuroimages. Comput. Biomed. Res 1996;29:162–173. [PubMed: 8812068]

Duyn JH, Yang Y, Frank JA, Mattay VS, Hou L. Functional magnetic resonance neuroimaging data acquisition techniques. NeuroImage 1996;4:S76–S83. [PubMed: 9345531]

Evans JW, Todd RM, Taylor MJ, Strother SC. Group specific optimisation of fMRI processing steps for child and adult data. NeuroImage 2010;50:479–490. [PubMed: 19962441]

Frahm J, Merboldt K-D, Hänicke W. Functional MRI of human brain activation at high spatial resolution. Magn. Reson. Med 1993;29:139–144. [PubMed: 8419736]

Galaburda AM, Rosen GD, Sherman GF. Individual variability in cortical organization: its relationship to brain laterality and implications to function. Neuropsychologia 1990;28:529–546. [PubMed: 2203994]

Gati JS, Menon RS, Ugurbil K, Rutt BK. Experimental determination of the BOLD field strength dependence in vessels and tissue. Magn. Reson. Med 1997;38:296–302. [PubMed: 9256111]

Geman S, Bienenstock E, Doursat R. Neural networks and the bias/variance dilemma. Neural Comput 1992;4:1–58.

Golay X, Pruessmann KP, Weiger M, Crelier GR, Folkers PJM, Kollias SS, Boesiger P. PRESTO-SENSE: an ultrafast whole-brain fMRI technique. Magn. Reson. Med 2000;43:779–786. [PubMed: 10861870]

Haase A, Frahm J, Matthaei D, Hänicke W, Merboldt K-D. FLASH imaging. rapid NMR imaging using low flip-angle pulses. J. Magn. Reson 1986;67:258–266.

Hansen LK, Larsen J, Nielsen FA, Strother SC, Rostrup E, Savoy R, Lange N, Sidtis J, Svarer C, Paulson OB. Generalizable patterns in neuroimaging: how many principal components? NeuroImage 1999;9:534–544. [PubMed: 10329293]

Hellier P, Barillot C, Corouge I, Gibaud B, Le Goualher G, Collins DL, Evans A, Malandain G, Ayache N, Christensen GE, Johnson HJ. Retrospective evaluation of intersubject brain registration. IEEE Trans. Med. Imag 2003;22:1120–1130.

Jezzard P, Balaban RS. Correction for geometric distortions in echo planar images from B_0 field variations. Magn. Reson. Med 1995;34:65–73. [PubMed: 7674900]

Koopmans PJ, Barth M, Norris DG. Layer-specific BOLD activation in human V1. Hum. Brain Mapp 2010;31:1297–1304. [PubMed: 20082333]

Krüger G, Glover GH. Physiological noise in oxygen-sensitive magnetic resonance imaging. Magn. Reson. Med 2001;46:631–637. [PubMed: 11590638]

Kustra R, Strother S. Penalized discriminant analysis of [^{15}O]-water PET brain images with prediction error selection of smoothness and regularization hyperparameters. IEEE Trans. Med. Imag 2001;20:376–387.

LaConte S, Anderson J, Muley S, Ashe J, Frutiger S, Rehm K, Hansen LK, Yacoub E, Hu X, Rottenberg D, Strother S. The evaluation of preprocessing choices in single-subject BOLD fMRI using NPAIRS performance metrics. NeuroImage 2003;18:10–27. [PubMed: 12507440]

Liu G, Sobering G, Duyn J, Moonen CTW. A functional MRI technique combining principles of echo-shifting with a train of observations (PRESTO). Magn. Reson. Med 1993;30:764–768. [PubMed: 8139461]

Lowe MJ, Sorenson JA. Spatially filtering functional magnetic resonance imaging data. Magn. Reson. Med 1997;37:723–729. [PubMed: 9126946]

Mansfield P. Multi-planar image formation using NMR spin echoes. J. Phys. C: Solid State Phys 1977;10:L55–L58.

Mansfield P, Coxon R, Glover P. Echo-planar imaging of the brain at 3.0 T: first normal volunteer results. J. Comput. Assist. Tomogr 1994;18:339–343. [PubMed: 8188896]

Mansfield P, Coxon R, Hykin J. Echo-volumar imaging (EVI) of the brain at 3.0 T: first normal volunteer and functional imaging results. J. Comput. Assist. Tomogr 1995;19:847–852. [PubMed: 8537514]

McGonigle DJ, Howseman AM, Athwal BS, Friston KJ, Frackowiak RSJ, Holmes AP. Variability in fMRI: an examination of intersession differences. NeuroImage 2000;11:708–734. [PubMed: 10860798]

Menon RS, Ogawa S, Tank DW, Ugurbil K. 4 Tesla gradient recalled echo characteristics of photic stimulation-induced signal changes in the human primary visual cortex. Magn. Reson. Med 1993;30:380–386. [PubMed: 8412612]

Mikl M, Marecek R, Hlustik P, Pavlicova M, Drastich A, Chlebus P, Brazdil M, Krupa P. Effects of spatial smoothing on fMRI group inferences. Magn. Reson. Imag 2008;26:490–503.

Miller KL, Smith SM, Jezzard P, Wiggins GC, Wiggins CJ. Signal and noise characteristics of SSFP FMRI: a comparison with GRE at multiple field strengths. NeuroImage 2007;37:1227–1236. [PubMed: 17706432]

Miller KL, Hargreaves BA, Lee J, Ress D, deCharms RC, Pauly JM. Functional brain imaging using a blood oxygenation sensitive steady state. Magn. Reson. Med 2003;50:675–683. [PubMed: 14523951]

Neggers SFW, Hermans EJ, Ramsey NF. Enhanced sensitivity with fast three-dimensional blood-oxygen-level-dependent functional MRI: comparison of SENSE-PRESTO and 2D-EPI at 3T. NMR Biomed 2008;21:663–676. [PubMed: 18189337]

Ogawa S, Menon RS, Tank DW, Kim S-G, Merkle H, Ellermann JM, Ugurbil K. Functional brain mapping by blood oxygenation level-dependent contrast magnetic resonance imaging: a comparison of signal characteristics with a biophysical model. Biophys. J 1993;64:803–812. [PubMed: 8386018]

Poline J-B, Mazoyer BM. Enhanced detection in brain activation maps using a multifiltering approach. J. Cereb. Blood Flow Metab 1994a;14:639–642. [PubMed: 8014211]

Poline JB, Mazoyer BM. Analysis of individual brain activation maps using hierarchical description and multiscale detection. IEEE Trans. Med. Imag 1994b;13:702–710.

Poline J-B, Worsley KJ, Evans AC, Friston KJ. Combining spatial extent and peak intensity to test for activations in functional imaging. NeuroImage 1997;5:83–96. [PubMed: 9345540]

Poser BA, Koopmans PJ, Witzel T, Wald LL, Barth M. Three dimensional echo-planar imaging at 7 Tesla. NeuroImage 2010;51:261–266. [PubMed: 20139009]

Pruessmann KP, Weiger M, Scheidegger MB, Boesiger P. SENSE: sensitivity encoding for fast MRI. Magn. Reson. Med 1999;42:952–962. [PubMed: 10542355]

Raj D, Paley DP, Anderson AW, Kennan RP, Gore JC. A model for susceptibility artefacts from respiration in functional echo-planar magnetic resonance imaging. Phys. Med. Biol 2000;45:3809–3820. [PubMed: 11131201]

Reilly JP. Peripheral nerve stimulation by induced electric currents: exposure to time-varying magnetic fields. Med. Biol. Eng. Comput 1989;27:101–110. [PubMed: 2689806]

Rosenfeld, A.; Kak, AC. Digital Picture Processing. Vol. vol. 2. Orlando, FL: Academic Press; 1982.

Sexton, J.; Swisher, J.; Tong, F.; Rogers, B.; Gatenby, JC.; Gore, JC. Development and evaluation of alternative imaging methods for fMRI at 7 Tesla. Proc. 18th Scientific Meeting of the ISMRM; Stockholm, Sweden. 2010. p. 1091

Sexton, JA. Ph.D. Thesis. Nashville, TN, USA: Vanderbilt University; 2010. Development and evaluation of alternative methods for functional magnetic resonance imaging at 7 Tesla.

Shaw ME, Moores KA, Clark RC, McFarlane AC, Strother SC, Bryant RA, Brown GC, Taylor JD. Functional connectivity reveals inefficient working memory systems in post-traumatic stress disorder. Psychiatry Res. Neuroimaging 2009;172:235–241.

Shaw ME, Strother SC, Gavrilescu M, Podzebenko K, Waites A, Watson J, Anderson J, Jackson G, Egan G. Evaluating subject specific preprocessing choices in multisubject fMRI data sets using data-driven performance metrics. NeuroImage 2003;19:988–1001. [PubMed: 12880827]

Shmuel A, Yacoub E, Pfeuffer J, Van de Moortele P-F, Adriany G, Hu X, Ugurbil K. Sustained negative BOLD, blood flow and oxygen consumption response and its coupling to the positive response in the human brain. Neuron 2002;36:1195–1210. [PubMed: 12495632]

Skudlarski P, Constable RT, Gore JC. ROC analysis of statistical methods used in functional MRI: individual subjects. NeuroImage 1999;9:311–329. [PubMed: 10075901]

Smith AT, Williams AL, Singh KD. Negative BOLD in the visual cortex: evidence against blood stealing. Hum. Brain Mapp 2004;21:213–220. [PubMed: 15038003]

Song AW, Wong EC, Hyde JS. Echo-volume imaging. Magn. Reson. Med 1994;32:668–671. [PubMed: 7808270]

Strother SC. Evaluating fMRI preprocessing pipelines. IEEE Eng. Med. Biol. Mag 2006;25:27–41. [PubMed: 16568935]

Strother SC, Anderson J, Hansen LK, Kjems U, Kustra R, Sidtis J, Frutiger S, Muley S, LaConte S, Rottenberg D. The quantitative evaluation of functional neuroimaging experiments: the NPAIRS data analysis framework. NeuroImage 2002;15:747–771. [PubMed: 11906218]

Strother S, La Conte S, Hansen LK, Anderson J, Zhang J, Pulapura S, Rottenberg D. Optimizing the fMRI data-processing pipeline using prediction and reproducibility performance metrics: I. A preliminary group analysis. NeuroImage 2004;23:S196–S203. [PubMed: 15501090]

Strother, S.; Oder, A.; Spring, R.; Grady, C. The NPAIRS computational statistics framework for data analysis in neuroimaging. In: Lechevallier, Y.; Saporta, G., editors. Proc. 19th Intl. Conf. on Computational Statistics: Keynote, Invited and Contributed Papers; Paris, France: Physica-Verlag, Springer; 2010. p. 111-120.

Thomas CG, Harshman RA, Menon RS. Noise reduction in BOLD-based fMRI using component analysis. NeuroImage 2002;17:1521–1537. [PubMed: 12414291]

Tootell RBH, Mendola JD, Hadjikhani NK, Liu AK, Dale AM. The representation of the ipsilateral visual field in human cerebral cortex. Proc. Natl. Acad. Sci. USA 1998;95:818–824. [PubMed: 9448246]

Triantafyllou C, Hoge RD, Krueger G, Wiggins CJ, Potthast A, Wiggins GC, Wald LL. Comparison of physiological noise at 1.5 T, 3 T and 7 T and optimization of fMRI acquisition parameters. NeuroImage 2005;26:243–250. [PubMed: 15862224]

Triantafyllou C, Hoge RD, Wald LL. Effect of spatial smoothing on physiological noise in high-resolution fMRI. NeuroImage 2006;32:551–557. [PubMed: 16815038]

van der Meulen P, Groen JP, Cuppen JJM. Very fast MR imaging by field echoes and small angle excitation. Magn. Reson. Imag 1985;3:297–299.

van der Meulen P, Groen JP, Tinus AMC, Bruntink G. Fast field echo imaging: an overview and contrast calculations. Magn. Reson. Imag 1988;6:355–368.

Vaughan JT, Garwood M, Collins CM, Liu W, DelaBarre L, Adriany G, Andersen P, Merkle H, Goebel R, Smith MB, Ugurbil K. 7T vs. 4T: RF power, homogeneity, and signal-to-noise comparison in head images. Magn. Reson. Med 2001;46:24–30. [PubMed: 11443707]

Weibull A, Björkman A, Hall H, Rosén B, Lundborg G, Svensson J. Optimizing the mapping of finger areas in primary somatosensory cortex using functional MRI. Magn. Reson. Imag 2008;26:1342–1351.

Weisskoff RM, Baker J, Belliveau J, Davis TL, Kwong KK, Cohen MS, Rosen BR. Power spectrum analysis of functionally-weighted MR data: what's in the noise? Proc. SMRM 1993;7

Worsley KJ, Friston KJ. Analysis of fMRI time-series revisited – again. NeuroImage 1995;2:173–181. [PubMed: 9343600]

Worsley KJ, Marrett S, Neelin P, Evans AC. Searching scale space for activation in PET images. Hum. Brain Mapp 1996;4:74–90. [PubMed: 20408187]

Wright PJ, Mougin OE, Totman JJ, Peters AM, Brookes MJ, Coxon R, Morris PE, Clemence M, Francis ST, Bowtell RW, Gowland PA. Water proton T_1 measurements in brain tissue at 7, 3, and 1.5 T using IR-EPI, IR-TSE, and MPRAGE: results and optimization. Magn. Reson. Mater. Phy 2008;21:121–130.

Yourganov G, Chen X, Lukic AS, Grady CL, Small SL, Wernick MN, Strother SC. Dimensionality estimation for optimal detection of functional networks in BOLD fMRI data. NeuroImage. in press.

Zhang J, Anderson JR, Liang L, Pulapura SK, Gatewood L, Rottenberg DA, Strother SC. Evaluation and optimization of fMRI single-subject processing pipelines with NPAIRS and second-level CVA. Magn. Reson. Imag 2009;27:264–278.

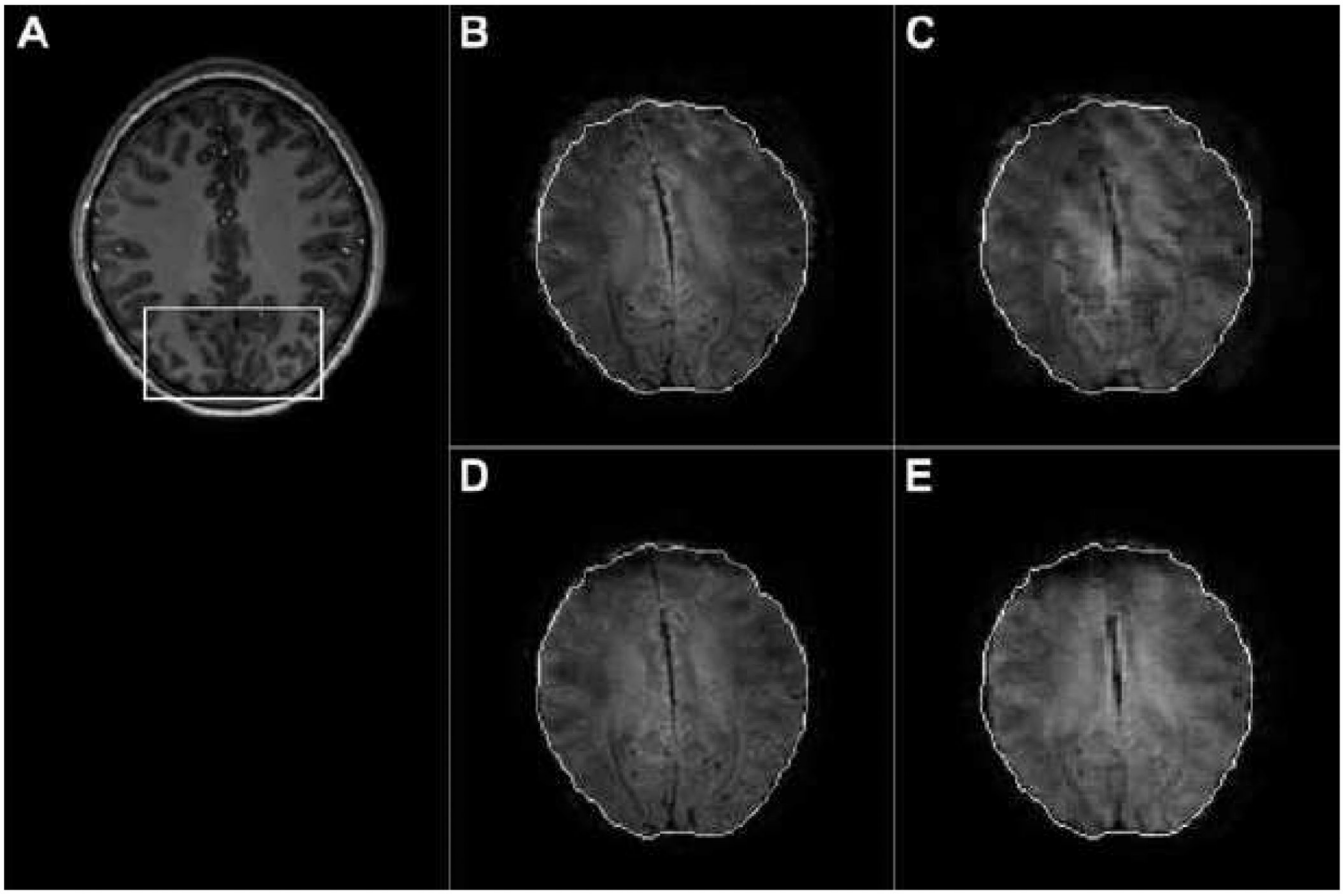

FIG. 1.

Images acquired from a representative subject. (**A**) High-resolution anatomical corresponding to the middle functional slice (parallel to the calcarine sulcus). The rectangle depicts the approximate intersection of the shim volume through this slice. (**B–E**): The middle functional slice from the first volume acquired using (**B**) EPI with 1.19 × 1.19 × 2 mm^3 voxels, (**C**) EPI with 2.19 × 2.19 × 2 mm^3 voxels, (**D**) FFE with 1.19 × 1.19 × 2 mm^3 voxels, and (**E**) PRESTO with 2.19 × 2.19 × 2 mm^3 voxels. The outline of the brain (excluding dura) in (A) is superimposed on functional images to better visualize geometric distortions in the phase-encode direction (left to right) both within and outside the shim volume for each acquisition sequence.

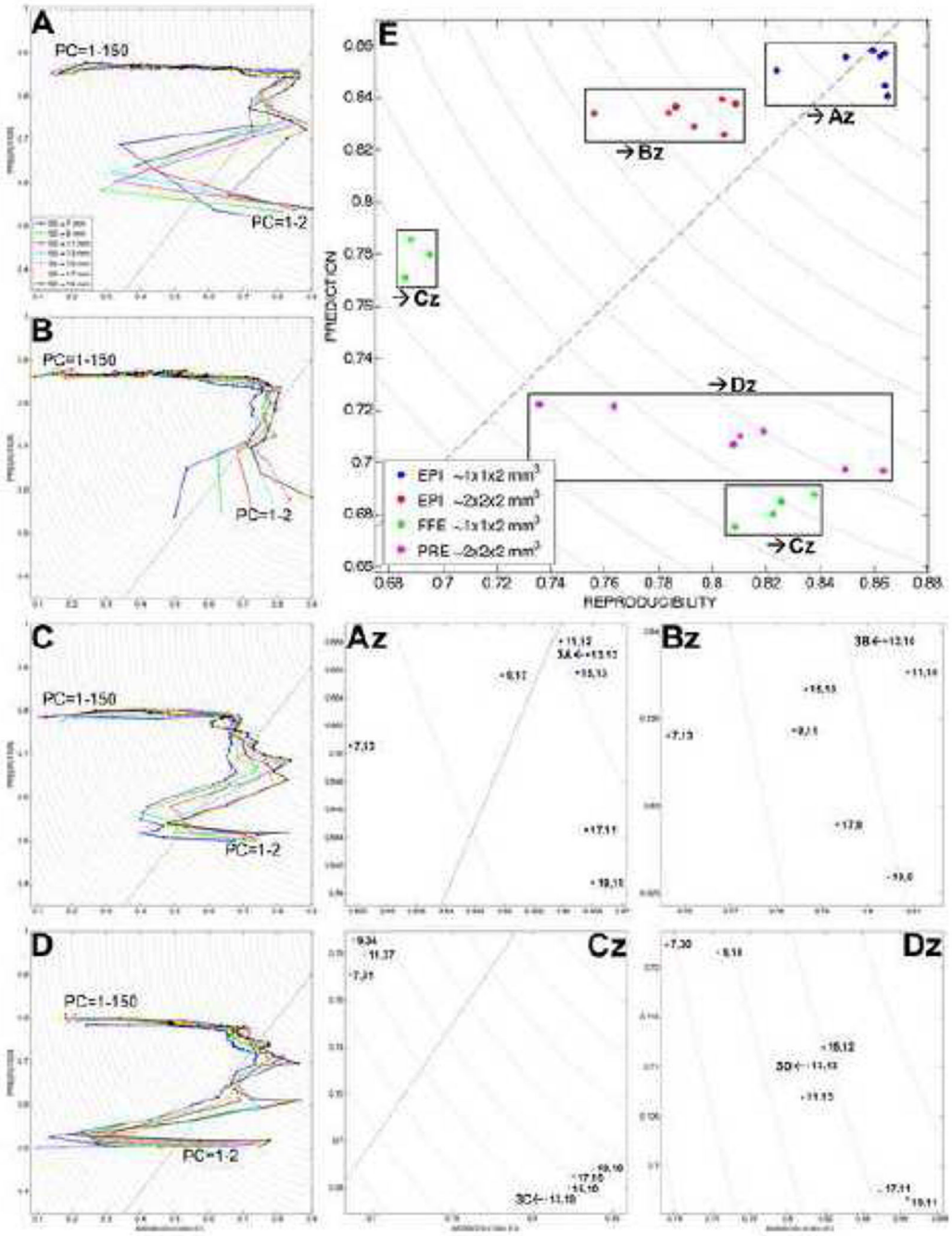

FIG. 2.

(**A**–**D**): Plots of prediction vs. reproducibility (*p*,*r*) for images acquired using (**A**) EPI with 1.19 × 1.19 × 2 mm^3 voxels, (**B**) EPI with 2.19 × 2.19 × 2 mm^3 voxels, (**C**) FFE with 1.19 × 1.19 × 2 mm^3 voxels, and (**D**) PRESTO with 2.19 × 2.19 × 2 mm^3 voxels. All possible combinations of 7 spatial smoothing kernel sizes (7, 9, 11, 13, 15, 17, 19 mm FWHM; see legend in A) and 52 ranges of principal components (PCs) (1–2, 1–3, …, 1–49, 1–50, 1–75, 1–100, 1–150) are considered, resulting in 364 (*p*,*r*) pairs for each of the four plots. In theory, noiseless fMRI data with a perfect model would map to the point (1,1) in the top right corner. Concentric dotted curves mark points that are equidistant to (1,1), and the dashed line marks equal prediction and reproducibility ($p = r$). A very low number of PCs

(1–2 or 1–3) can result in high reproducibility but low prediction from artifacts, illustrating why reproducibility alone is typically insufficient to identify the underlying dimensionality of the data. Increasing the number of PCs has a similar impact on prediction and reproducibility across kernel sizes and acquisition strategies: (*p*,*r*) increases toward (1,1) in a complicated manner, achieves one or more points that are close to (1,1), and then reproducibility decreases toward zero while prediction remains virtually unchanged. (**E**): For each of the 28 curves in (A–D), the (*p*,*r*) point with the shortest Euclidean distance to (1,1) is identified. (**Az–Dz**): The clusters outlined in (E) are magnified to better visualize the relative distance between points. The two numbers beside each point denote smoothing kernel size and number of PCs. The arrows and additional subplot labels (e.g., →3A) indicate which four (*p*,*r*) points correspond to the four activation maps in Fig. 3.

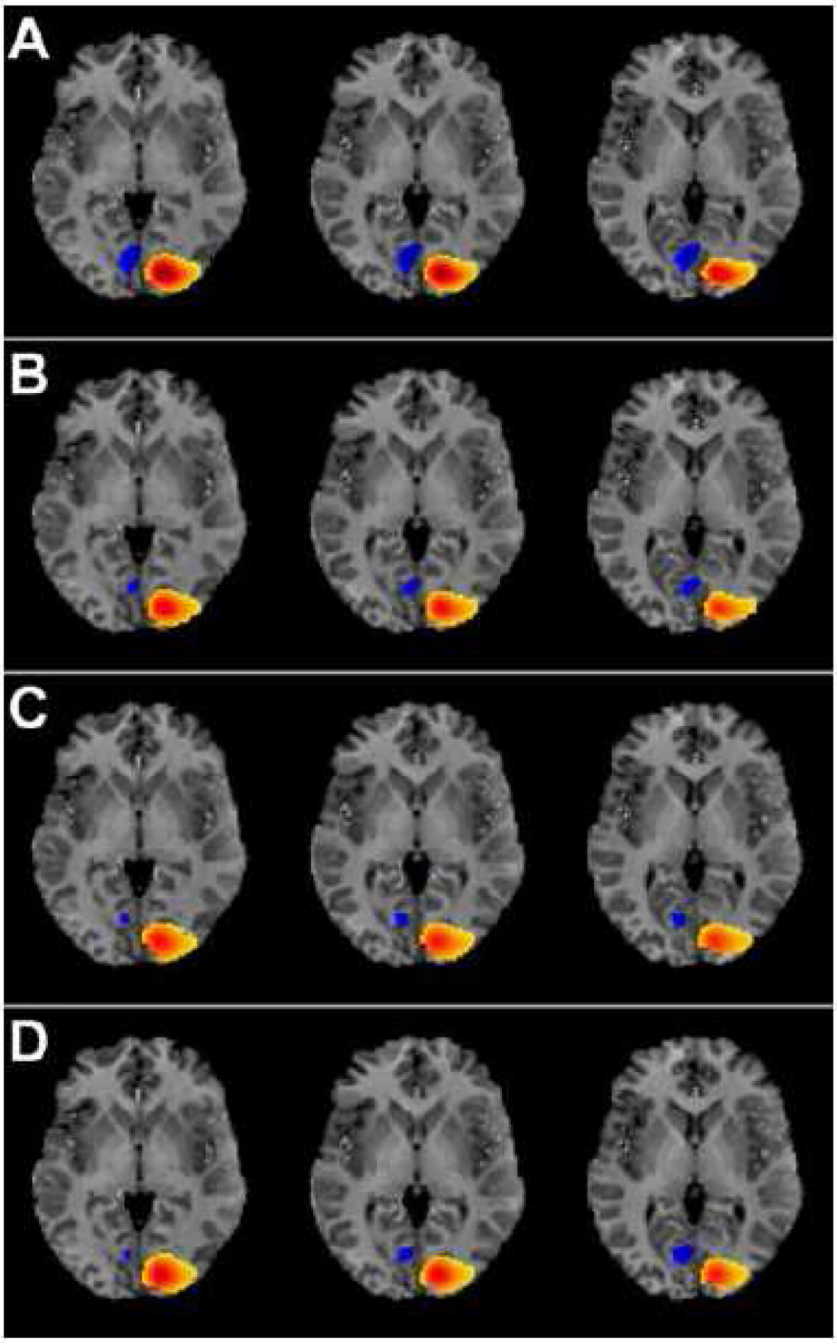

FIG. 3.

Group activation maps associated with optimal (*p*,*r*) (identified by arrows in Fig. 2(Az–Dz)) for: (**A**) high-resolution EPI with PCs=1–12, (**B**) low-resolution EPI with PCs=1–10, (**C**) FFE with PCs=1–10, and (**D**) PRESTO with PCs=1–13. Data were processed with a spatial smoothing kernel of 13 mm FWHM. Maps are presented with a common threshold of $|z| > 5$ and dynamic range from $z = -6.670$ (blue) to $z = 18.99$ (dark red).

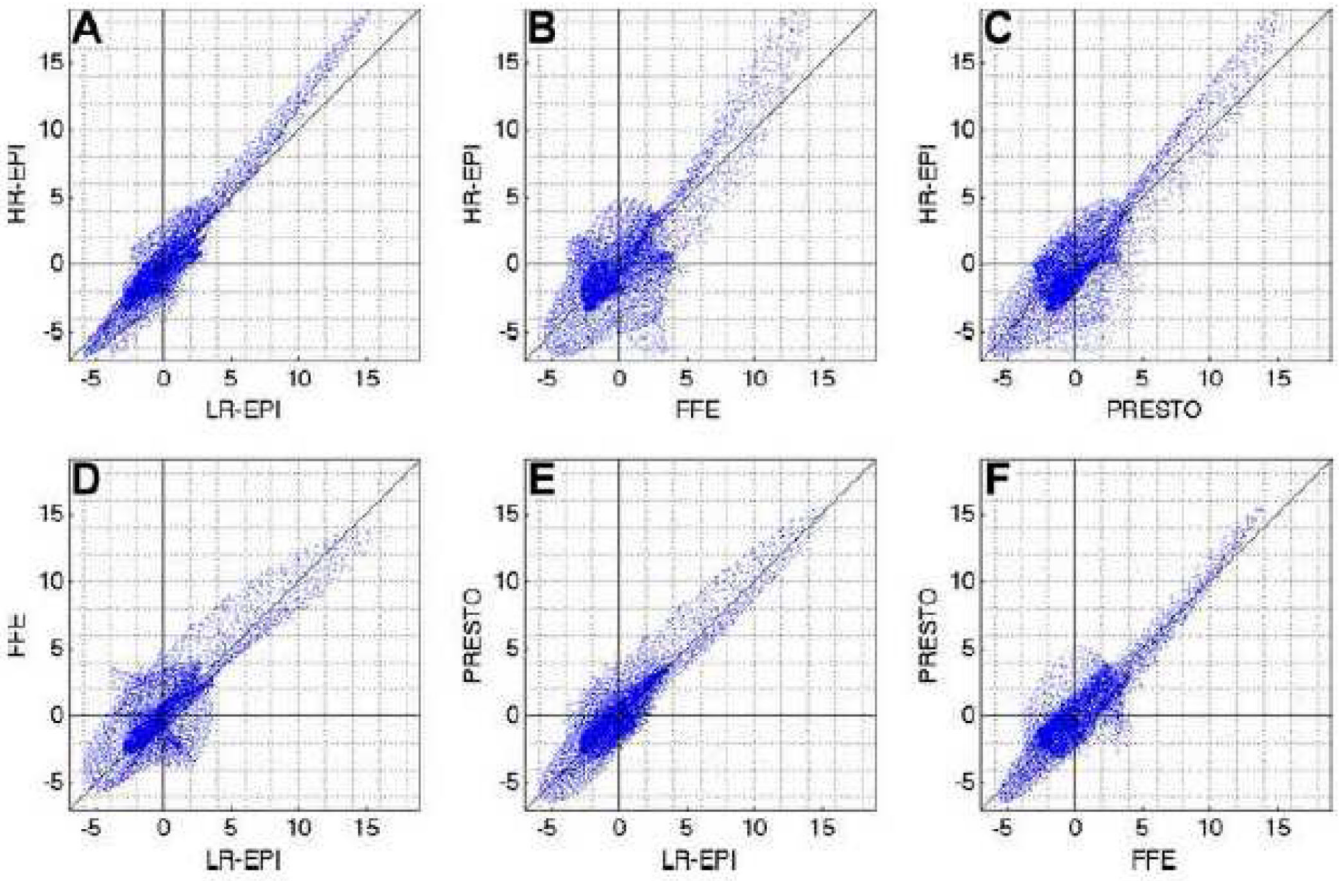

FIG. 4.

Voxel-wise comparisons of z-scores for unthresholded activation maps in Fig. 3: (**A**) high-resolution (HR)-EPI vs. low-resolution (LR)-EPI; (**B**) HR-EPI vs. FFE; (**C**) HR-EPI vs. PRESTO; (**D**) FFE vs. LR-EPI; (**E**) PRESTO vs. LR-EPI; and (**F**) PRESTO vs. FFE. A point (representing one voxel) above the line of unity reflects a voxel exhibiting a higher group z-score with the acquisition sequence labeled on the vertical axis than the acquisition sequence labeled on the horizontal axis, and vice versa.

TABLE 1

fMRI acquisition parameters for four sequences.

	SINGLE-SHOT		MULTI-SHOT	
pulse sequence	**2D EPI**		**3D FFE**	**3D PRESTO**
k-space matrix	176 × 176	96 × 96	176 × 176	96 × 96
voxel size (mm^3)	1.19 × 1.19 × 2	2.19 × 2.19 × 2	1.19 × 1.19 × 2	2.19 × 2.19 × 2
# of slices	12			
TE (ms)	28			
TR (ms)	2000		44.45	22.22
vol. acq. time (ms)	2000			1000
# of volumes	96			192
flip angle (deg)	87		17	12
SENSE factor (R)	3.2			
echo train length	57	33	19	11
Freq/PE BW (Hz)	1474.6 / 20.0	1766.4 / 42.5	997.1 / 42.6	2930.4 / 142.5

TABLE 2

Mean percentage z-score increase across highly significant voxels (z > 7) for the acquisition sequence in the numerator compared to the acquisition sequence in the denominator (HE = HR-EPI; LE = LR-EPI; F = FFE; P = PRESTO) for each spatial smoothing kernel considered.

7 mm	9 mm	11 mm	13 mm	15 mm	17 mm	19 mm
$\frac{HE}{LE}$=18.3	$\frac{HE}{LE}$=22.2	$\frac{HE}{LE}$=17.4	$\frac{HE}{LE}$=20.3	$\frac{HE}{LE}$=23.6	$\frac{HE}{LE}$=24.2	$\frac{HE}{LE}$=21.0
$\frac{HE}{F}$=43.3	$\frac{HE}{F}$=57.2	$\frac{HE}{F}$=57.6	$\frac{HE}{F}$=19.8	$\frac{HE}{F}$=13.6	$\frac{HE}{F}$=10.5	$\frac{HE}{F}$=7.39
$\frac{HE}{P}$=19.4	$\frac{HE}{P}$=23.5	$\frac{HE}{P}$=16.0	$\frac{HE}{P}$=15.1	$\frac{HE}{P}$=13.8	$\frac{HE}{P}$=2.09	$\frac{P}{HE}$=4.84
$\frac{LE}{F}$=19.5	$\frac{LE}{F}$=26.1	$\frac{LE}{F}$=32.7	$\frac{F}{LE}$=7.50	$\frac{F}{LE}$=14.5	$\frac{F}{LE}$=14.8	$\frac{F}{LE}$=13.8
$\frac{P}{LE}$=2.91	$\frac{P}{LE}$=3.56	$\frac{P}{LE}$=6.86	$\frac{P}{LE}$=9.73	$\frac{P}{LE}$=12.9	$\frac{P}{LE}$=24.3	$\frac{P}{LE}$=26.4
$\frac{P}{F}$=25.7	$\frac{P}{F}$=33.1	$\frac{P}{F}$=40.9	$\frac{P}{F}$=4.55	$\frac{P}{F}$=0.21	$\frac{P}{F}$=7.91	$\frac{P}{F}$=9.62